Mechanism and performance of a hydrofoil bubble generator utilized for bubbly drag reduction ships

Yuichi Murai[*1], Haruki Sakamaki[1], Ichiro Kumagai[2], Hyun Jin Park[1], and Yuji Tasaka[1]

1 Laboratory for Flow Control, Faculty of Engineering, Hokkaido University, Sapporo, 060-8628, Japan

2 School of Science and Engineering, Meisei University, Hino, Tokyo, Japan

**Corresponding author: Y. Murai, Dr., E-mail: murai@eng.hokudai.ac.jp*

Abstract

Following the success of bubbly drag reduction for marine vessels by hydrofoil bubble generators (Kumagai et al., 2015), we conducted two kinds of experiments to specify and improve its working principle. Firstly, PIV measurement was carried out to elucidate the flow structure around a hydrofoil running beneath a free surface. Froude number dependence of the anti-stall characteristics and cancellation of vertical pressure gradient above the hydrofoil were confirmed, which entrain the atmospheric air into water flow. Secondly, we mounted the hydrofoil to a model ship that runs in a 100-m-towing facility and found three different two-phase flow patterns in realizing bubble generation. Volume flow rate of generated bubbles increased with the ship speed to the power of greater than two, thus wall-occupation fraction of bubbles also increases with the ship speed. Furthermore, hydrofoil drag during bubble generation was measured and used to estimate net power-saving, having proved advantage of the hydrofoil bubble generator for long ships at high speed conditions.

Keywords: Bubbly drag reduction, hydrofoil bubble generator, air lubrication, two-phase flow

1. Introduction

Air lubrication of ship hull saves fuel consumption and thus greenhouse gas emission. The saving is realized by reduction of wall shear stress due to mixing of air inside turbulent boundary layer. In the last two decades, air lubrication ships have shifted to practical stage in the marine transport industry as reported by American Bureau of Shipping (2019). Up to now, at least 21 large vessels employed air lubrication system, among which the authors' group contributed to four vessels in basic design. As Ceccio (2010) reported in his review, there are three types of air's role in drag reduction classified by status of air phase distribution: stagnant air cavity by providing a wide concave bottom beneath the hull surface (air-cavity drag reduction, ACDR), injection of air layer to separate from water flow (air-layer drag reduction, ALDR), and injection of small bubbles that suppress turbulence in the boundary layer (bubbly drag reduction, BDR). For ALDR and BDR, air needs to be injected at a certain volume flow rate. For ACDR, some air blowing maintains the level of air-water interface inside the cavity. A problem in these techniques is extra power consumed for air injection against hydrostatic pressure. Among them, ALDR is categorized as a technique realizing high local drag reduction rate over 50% with void fraction higher than 50% given to the boundary layer. It is applicable to speed-up the marine vessel at a given propulsion power. To optimize and stabilize the performance of ALDR, adjustment of air injection has been reported to effectively cover wide area of the hull surface

(Mäkiharju et al., 2017; Jang et al., 2014; Cucinotta et al., 2017).

In contrast, BDR expects drag reduction rate up to 30% with small amount of air injection in the status of dispersed bubbles. To keep the dispersed state, mean void fraction in the boundary layer is restricted lower than 20%. Fluid mechanics of BDR is quite complex and sensitive to bubble size relative to the boundary layer thickness. Nevertheless, two outstanding advantages in BDR promote practical use. One is sensitivity of drag reduction, often taking from 3 to 10 in power gain; the power gain is defined by the power-saving relative to the power consumed for bubble injection (Murai, 2014). The other is applicability not only to flat-bottom hull but also to inclined and vertical surfaces as bubbles are generated small enough, i.e. bubble rise speed becomes much slower than the ship speed. High power gain of BDR depends on controllability of bubble size (Moriguti and Kato 2002; Murai et al., 2007; Oishi and Murai, 2014). However, bubble size in a long downstream distance is not deterministically controlled only by the bubble generator. Bubbles will naturally be a few mm in size at mean shear rate of 100 s^{-1} (Park et al. 2016), and sub-mm size at 1000 s^{-1} (Kitagawa et al., 2005; Sanders et al., 2006). It also depends on wettability of the wall (Kitagawa et al., 2019) and spontaneous bubble-clustering along the wall (Oishi et al., 2019). Instead of bubble size control, use of artificial void waves were reported to promote drag reduction (Park et al., 2015; Park et al., 2018). This technique utilizes spatial renewal effect of turbulent boundary layer with repetitive passage of void waves. For microbubble regime of BDR, which means bubbles of less than 100 μm in size, elementary vortices in turbulence are suppressed by their capturing microbubbles to cause very sensitive drag reduction (Zhen and Hassan, 2006; Hara et al., 2011; Park et al., 2019).

Another important effort to improve BDR is reduction of power consumed for bubble generation. It depends on draft of the hull and pressure loss in generating bubbles, which greatly affect the net power-saving. In our previous paper (Kumagai et al., 2015), we reported usefulness of hydrofoil-type bubble generator for ship drag reduction. With this device, bubbles are naturally generated due to pressure lowering around the hydrofoil (Murai and Takahashi, 2008; Takahashi and Murai, 2014). Any blower and compressor for air transport to underwater are unnecessary up to a certain draft of bubble injection (typically 4 to 5 m at a cruising speed of 10-15 knots). Although attachment of hydrofoils makes total ship drag increase, overall drag reduction by the bubbles exceeds it when applied for long vessels. The effectiveness was proved by applications to three different real vessels; a 13-m-long fishing boat, a 64 m-long passenger ferry, and a 85-m-long cargo. Net drag reduction in average was around 10% as the result of long-term fuel consumption rate examined in commercial shipping operation. Around a half of total ship drag originates from the form drag, thus 10% of fuel-saving deduces 20% of frictional drag reduction. All details of these sea trials were elaborated in our past paper (Kumagai et al., 2015), and also in the book edited by Pavlov et al., (2020).

Since 2015, our team conducted a series of experiments to seek further potential of improvement. Purpose of the experiment is to find answers for the following questions.

i) Why can hydrofoil effectively generate bubbles? How do air and water merge to be mixed as bubbles behind the hydrofoil? There must be an intrinsic mechanism of two-phase flow around the hydrofoil.

ii) What kind of hydrofoil shape works better as a bubble generator? How is the best angle of attack determined? There must be an optimum point regarding hydrofoil lift/drag ratio as water surface approaches the hydrofoil.

iii) How the resultant bubble volume flow rate of bubbles can be estimated? Since bubbles are generated around the hydrofoil passively with ship advance, accurate theory must be established as two-phase fluid dynamics helping

future designs for improvement.

Recently, some trials of CFD simulation for our hydrofoil system was reported by Zhang et al. (2018) and Yanuar et al. (2020). They clarified the working principle successfully but in a limited range of operation condition. In this paper, we present two kinds of experimental results answering for these questions. One is PIV (particle image velocimetry) measurement of water flow around the hydrofoil as water surface approaches it. This enables us to understand how the hydrofoil induces surrounding liquid flow interacting with deformation of free surface. The other is measurement of bubble generation performance as the hydrofoil was mounted to a model ship that runs in a 100-m-long towing facility. This offers energy efficiency of bubble generation evaluated by drag acting on the hydrofoil in operation bubble generation.

2. Flow field around a hydrofoil with free surface

Interaction between flow around a hydrofoil and a free surface was studied by Fuwa et al. (1980) and Duncan (1983). They reported on deformation of the free surface and resultant hydrodynamic forces acting on the hydrofoil. At Froude number larger than 2, the free surface sharply caves down behind the hydrofoil to occur wave-breaking in the downstream region. Similar phenomena arise also for a circular cylinder running close to a free surface, in which periodic vortex shedding promotes wave-breaking (e.g., Sheridan and Rockwell, 1997; Reichl et al., 2005; Kumagai et al., 2011). In this chapter, we present flow visualization and pressure distribution around the hydrofoil.

2-1. Experimental set-up

We used a 5-m-long open towing water tank as shown in **Fig. 1(a)**. A hydrofoil was fixed on a carriage above the water via a connecting rod, which runs horizontally at a controlled speed, U. A green laser generator (NdYAG, 532 nm) and a high-speed camera are mounted on the moving carriage. Dimension of the hydrofoil and coordinate system are defined as **Fig. 1(b)**; C is cord length of the hydrofoil (C= 50 mm), and h denotes the depth of the hydrodynamic center of the hydrofoil from the free surface. Angle of attach, α, is defined by the relative angle between the cord direction and the inflow vector. Following non-dimensional numbers are used to characterize the flow field.

$$Re = CU / \nu , \tag{1}$$

$$Fr_C = U / \sqrt{gC} , \tag{2}$$

$$h^* = h / C , \tag{3}$$

where ν is kinematic viscosity of water. Re is Reynolds number of the hydrofoil, Fr_c is Froude number defined by the cord length of the hydrofoil. g is acceleration of gravity. Since free surface behavior depends on the hydrofoil depth h, Eq. (3) defines non-dimensional depth as a geometric similarity parameter. Experimental conditions are summarized in **Table 1**.

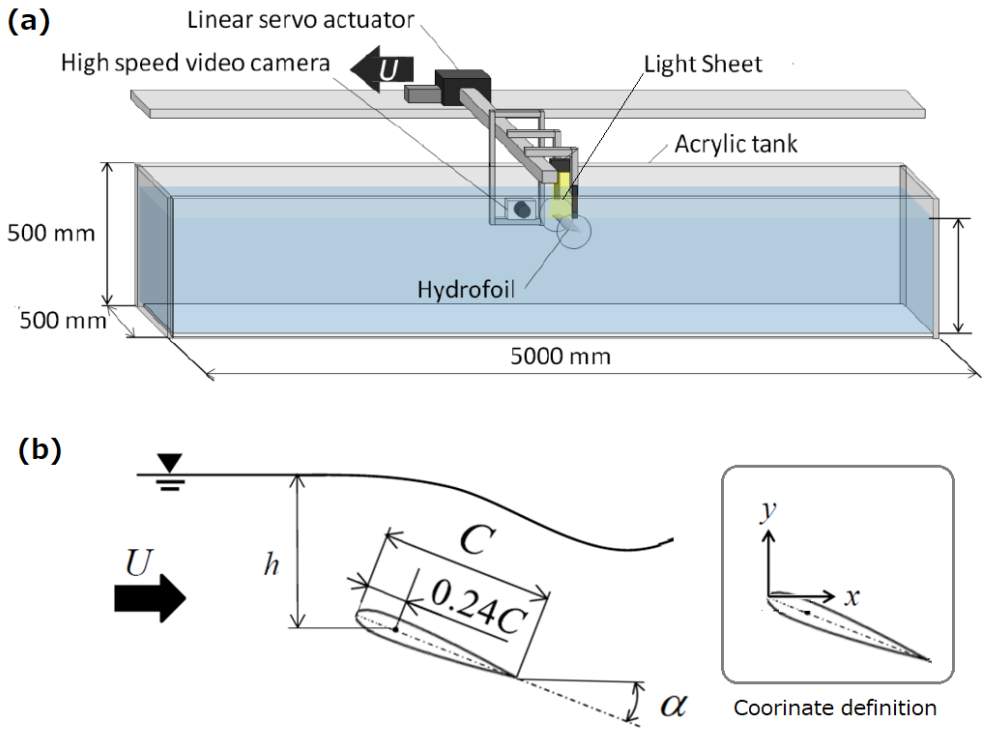

Fig. 1 Towing experiment using an open water tank. (a) Schematic of the set-up constitute of carrying stage driven by a linear slider, on which the hydrofoil and PIV window moves together, (b) definition of geometrical parameters of the hydrofoil running close to the free surface

Table 1

Experimental conditions of hydrofoil towing tests

	Symbol	Value	unit
Towing speed	U	0.35 – 1.25	m/s
Angle of attack	α	20	degree
Water depth (Hydrofoil)	h	12, 25, 50	mm
Temperature		13.5	°C
depth ratio	h^*	0.25 – 1.00	-
Reynolds number	Re	1.4×10^4 – 5.2×10^4	-
Froude number (c)	Fr_c	0.5, 1.0, 1.6, 1.8	-
Frame rate	f	500	fps
Size	$w \times h$	1280 × 1024	pixel
Resolution	r	0.102	mm/pixel

2-2. Visualization of flow and interface

Fig. 2 presents flow patterns around a hydrofoil visualized by tracer particles seeded in water. The particles are made of high-porous polymer of 1010 kg/m^3 in density and 90 μm in mean diameter (Diaion, Mitsubishi Chemical Co. Ltd, Japan). Asymmetric NACA4412 hydrofoil was used at angle of attack was set at α=20 degree in this demonstration.

Reynolds number was ranged in (1.4 - 5.2)x10^4. In case of infinite fluid without free surface, the hydrofoil of α=20 occurs flow separation on this *Re* number order. In deep setting of the hydrofoil by h^*=1.00 (see the top four panels), the flow separation occurs from the leading edge at Fr_c=0.5, 1.6, and 1.8. This agrees with flow separation condition in an infinite fluid. In shallow setting at h^*=0.25-0.50, flow separation ceases at Fr_c=0.5-1.0. Instead, a recirculation region takes place beneath the free surface at Fr_c=0.5. On shallow high-speed conditions at h^*=0.25 and $Fr_c \geq 1.6$, separation region expands upward together with an uplift of the free surface. An interesting finding is that no separation occurs at Fr_c=1.0 in any case of hydrofoil depth examined. This is attributed to balancing between the negative pressure and the positive hydrostatic pressure inside the layer flowing above the hydrofoil. Namely, downhill of the water over the hydrofoil suppressed flow separation, of which phenomenon is understandable analogously to torrential flow so called. The detail internal structure will be shown later at section 2-5.

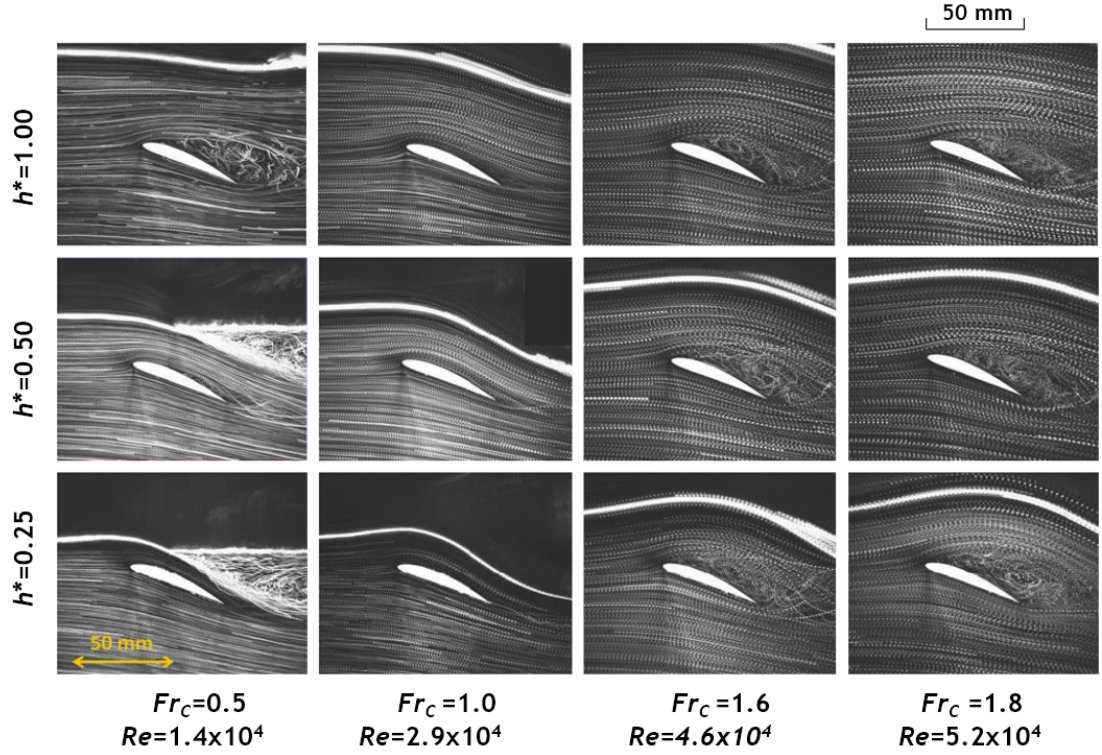

Fig. 2 Path-line visualization of flow around the hydrofoil influenced by the position of upper free surface h^* and the Froude number Fr_C. The region of path-lines tangled indicates stall or recirculation region above the hydrofoil.

2-3. PIV-based pressure field measurement

Motion of tracer particles is analyzed by PIV to obtain velocity vector field (**Fig. 3 (a)**). We use Poisson equation of pressure to estimate pressure field around the hydrofoil, given by

$$\frac{\partial^2 p}{\partial x^2}+\frac{\partial^2 p}{\partial y^2}=-\rho\left[\frac{\partial}{\partial x}\left(u\frac{\partial u}{\partial x}+v\frac{\partial u}{\partial y}\right)+\frac{\partial}{\partial y}\left(u\frac{\partial v}{\partial x}+v\frac{\partial v}{\partial y}\right)\right], \tag{4}$$

where u and v are the velocity components in x and y directions, respectively. ρ is density of fluid. To improve the velocity resolution required to calculate the r.h.s. of Eq. (4), we took median filter and time-average of raw data of PIV. This raises the resolution from 3-bit to 8-bit, enough to compute the second derivative of the velocity components.

Further additional filtering such as enforcing continuity was not applied. Boundary conditions of pressure on the surface of the hydrofoil and on the PIV window frame were given by gradient-free condition in each perpendicular direction. In cases of free surface involved in PIV window, pressure on the free surface was fixed as atmospheric pressure. Corresponding result (**Fig 3(b)**) shows good agreement to many past literatures, i.e. the lowest pressure takes place above the suction surface and pressure rise occurs near the leading edge on the bottom surface.

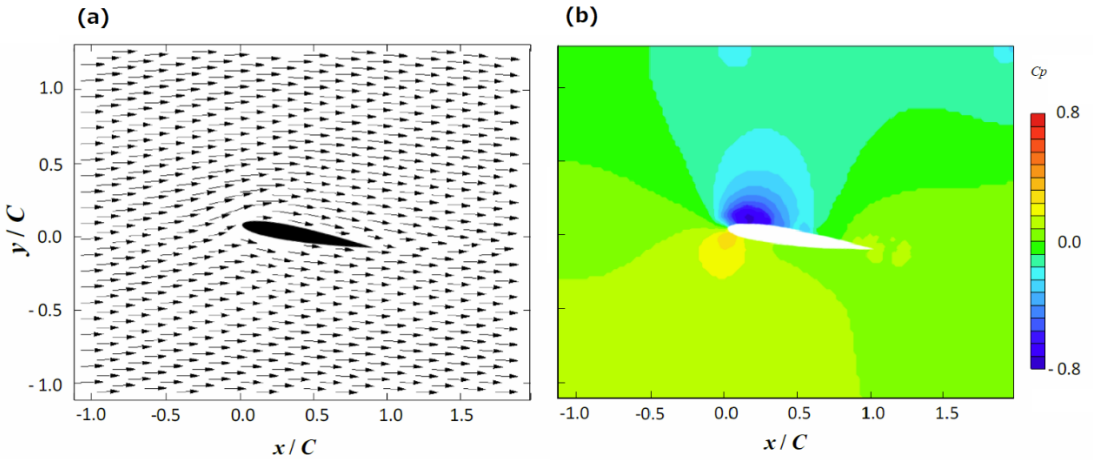

Fig. 3 PIV based pressure field around NACA0012 for the angle of attack at α=10 degree. (a) Water velocity vector distribution obtained by PIV, (b) pressure contour computed from the PIV data

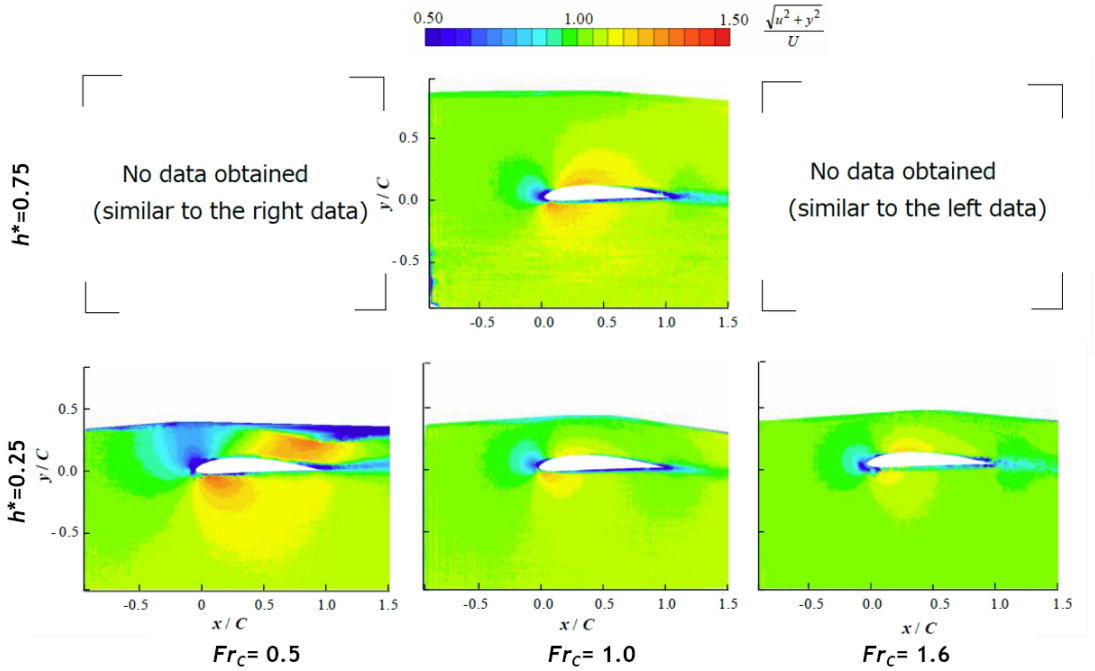

Fig. 4 Velocity magnitude distributions of flow around NACA4412 hydrofoil at angle of attack α=0, changing with dimensionless depth h^* and Fr number. Re number dependence was insignificant and omitted for h^*=0.75.

Using this method, relationship between the flow velocity and the pressure field is compared with changing the hydrofoil depth h^* and Fr_c number. **Fig. 4** depicts distribution of velocity magnitude normalized by the towing speed U. Angle of attack α is set at zero in these cases. At h^*=0.75, velocity increases on the both surfaces of the hydrofoil

(see red yellow and regions). Shallowing the hydrofoil to h^*=0.25, the velocity takes different trend dependent on Fr_c number. At Fr_c =0.5, the increase of velocity above the hydrofoil shifts to rear edge. This causes a thin stagnant layer at the water surface (see blue layer). At Fr_c =1.0 and Fr_c =1.6, the increase of velocity is relaxed and becomes smaller than that in the case of h^*=0.75. Since the results were judged similar for h^*=0.75 at Fr_C=0.5 and Fr_C =1.6, PIV analysis for them were omitted.

Corresponding pressure fields are shown in **Fig. 5**. Here the pressure is defined as dynamic pressure directly obtained by the Poisson equation, Eq. (4), i.e. hydrostatic pressure component is excluded. Pressure inside the gas is expressed by zero in gauge pressure. Compared with negative pressure above the hydrofoil at h^*=0.75, shallow setting at h^*=0.25 causes a relaxed distribution. At Fr_c=0.5, negative pressure is amplified rather on the bottom surface. Furthermore, a high-pressure tail emerges behind the trailing edge, oppositely to that at the deep setting. This is caused by gravity-driven water downhill merges with the flow come from the bottom. At Fr_c=1.0, stagnation pressure-rise is intensified around the leading edge, and it is calmed at Fr_c=1.6. This infers that stagnation region expands with narrowing of the flow above the hydrofoil. The data was not obtained for h^*=0.75 at Fr_c=0.5 and Fr_c=1.6 because of little difference from Fr_C=1.0 observed.

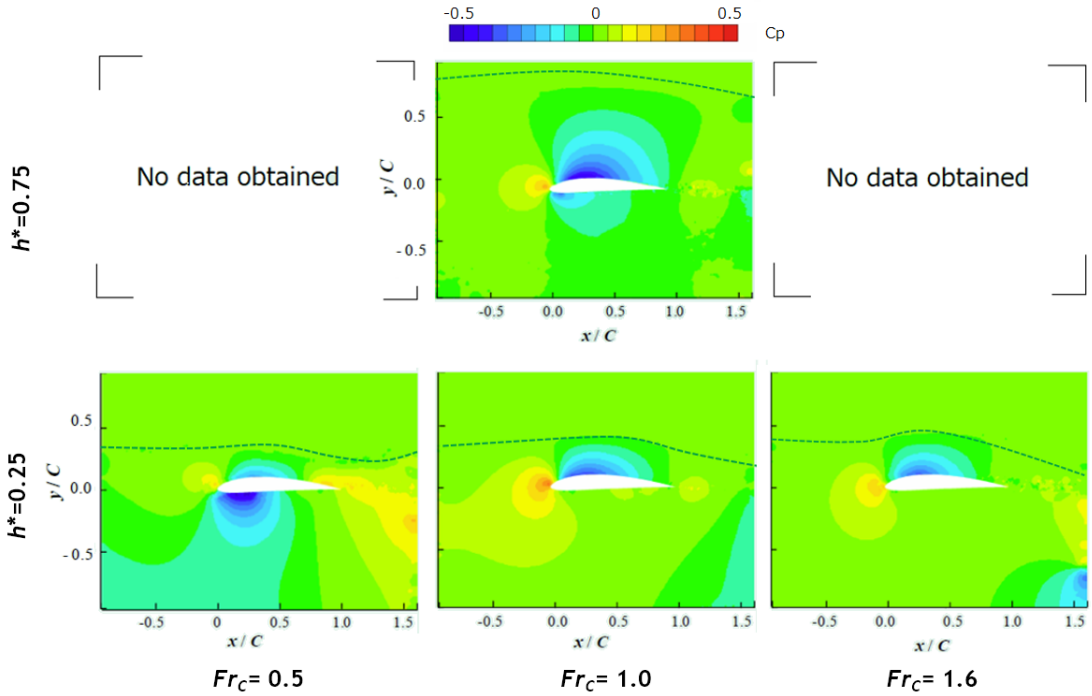

Fig. 5 Dynamic pressure distributions of flow around NACA4412 hydrofoil at angle of attack α=0, changing with *Fr* number. Dashed line indicates the water surface averaged in time. Color above the free surface is intentionally left to demonstrate occupation of atmospheric pressure which is zero in dynamic pressure.

2-4. Pressure profiles around the hydrofoil

Pressure profiles around a hydrofoil moving close to a free surface were measured in the past by Fuwa and Ishizaka (1980) (reported in Japanese). Their purpose of research was utilizing the data for performance examination of a hydrofoil boat. We refer to their data and compared with our data as shown in **Fig. 6**. Hydrofoil shape and *Re* number

are the same as theirs. Our data are generally in good agreement with their data of the suction side. For examples, the negative pressure on the suction surface is relaxed with decrease of h^* (**Fig. 6(a)**). A certain difference from the data of Fuwa and Ishizaka (1980) is seen on the bottom surface, which come from the difference of the total depth of the tank. Our tank is 0.5 m in height while their tank was 3.5 m high. As for bubble generator, we are interested only the suction surface of the hydrofoil. At low flow speed of Fr_c=0.5, it causes decreasing pressure gradient on the suction surface while increasing pressure gradient occurs on the bottom sufface (**Fig. 6(b)**).

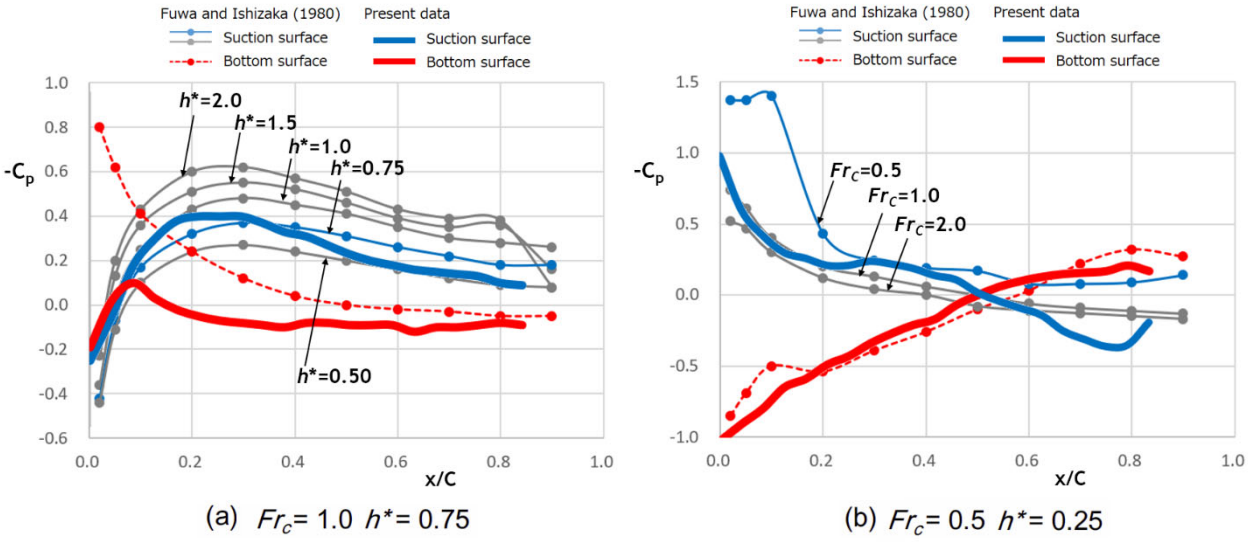

Fig. 6 Pressure coefficient profiles of NACA4412 at α=0 degree changing with hydrofoil depth h^* and Froude number Fr_C, compared with pressure tap measurement by Fuwa and Ishizaka (1980).

2-5. Absolute pressure distribution

Eq. (4) gives only the dynamic pressure component. To estimate the absolute pressure distribution, we add hydrostatic pressure distribution as

$$p = p_d + p_h, \quad p_h = \begin{cases} p_a & y \geq y_a(x) \\ p_a + \rho g\left[y_a(x) - y\right] & y < y_a(x) \end{cases} \tag{5}$$

where p, p_d and p_h are absolute, dynamic and hydrostatic pressure components, respectively. p_a is atmospheric pressure in air phase, and $y_a(x)$ denotes local height of free surface as a function of the horizontal coordinate x.

Fig. 7 represents two cases of the results, where top and bottom panels correspond to the dynamic pressure and absolute pressure, respectively. At Fr_c=0.5, dynamic pressure component is mostly overcome by the hydrostatic pressure in the absolute pressure distribution. Water flow above the hydrofoil is dominated by the hydrostatic pressure gradient, which takes a gradient oppositely to the dynamic pressure. Resultantly, the pressure gradient above the hydrofoil disappears at Fr_c=1.0, i.e. cancellation of the vertical pressure gradient. According to the streamline-curvature theorem, the cancellation condition is explained by the equation below,

$$\left\langle \frac{dp}{dy} \right\rangle = \rho \frac{U^2}{R} - \rho g = \rho g \left(\frac{U^2}{gR} - 1 \right) = g\left({Fr_R}^2 - 1 \right), \quad Fr_R = \frac{U}{\sqrt{gR}} = \sqrt{\frac{C}{R}} Fr_C, \tag{6}$$

where R stands for a representative curvature radius of the flow above the hydrofoil. Fr_R is Froude number defined

with R. The equation tells that the vertical pressure gradient is cancelled at Fr_R=1. Here, C/R ~1 for the hydrofoil of NACA4412, therefore the cancellation occurs at Fr_c=1. This creates a local pressure lower than the atmospheric pressure in a region on the suction surface, especially for the high-angled asymmetric hydrofoil (see **Fig. 7** at Fr_c=1). This feature is important when the hydrofoil is used as a bubble generator. Once bubbles enter this region, they are trapped on the surface to alter the hydrofoil performance. We show this phenomenon in the next section.

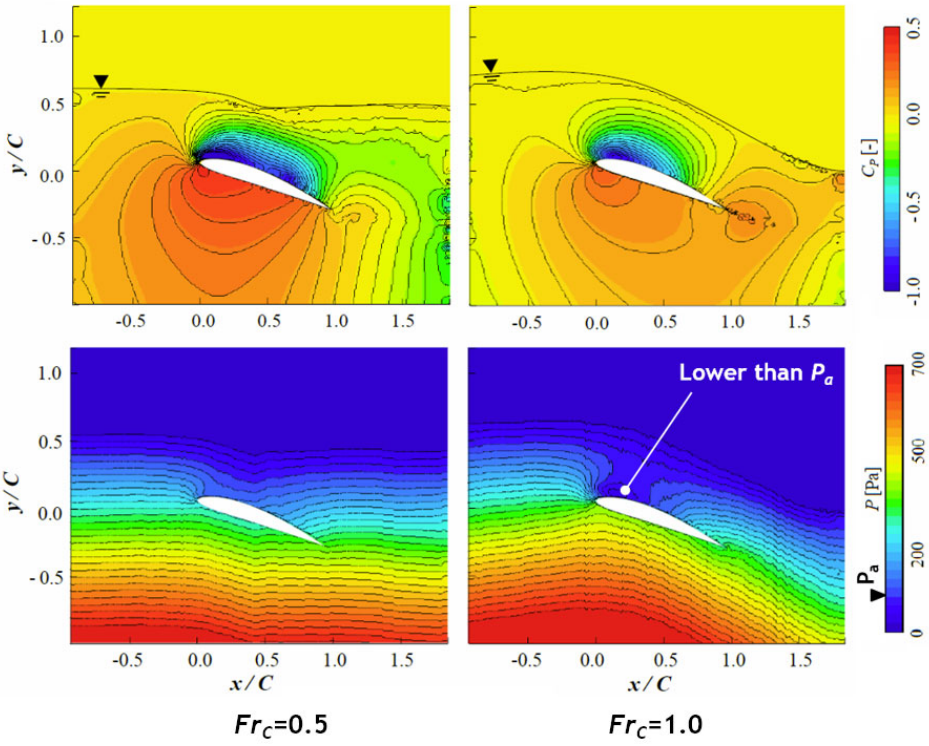

Fig. 7 Non-dimensional dynamic pressure and absolute pressure field of flow around NACA4412 hydrofoil at angle of attack α=20 degree. The absolute pressure has a unit of Pa and is the sum of hydrostatic pressure, atmospheric pressure on the free surface and the dynamic pressure reconstructed by $C_p\rho U^2/2$.

3. Towing model ship experiment

Based on understanding the flow characteristics mentioned above, we equipped the hydrofoil on a model ship to measure the bubble generation performance.

3-1. Experimental set-up

The model ship experiment was carried out in a 100 m long towing tank facility in Hiroshima University, Japan. The tank is 3.5 m depth and 8.0 m wide. The view of the experiment is shown in **Fig. 8**. Our model ship was 4 m long in total, made of fully transparent acrylic resin to enable optical measurement of bubbles both from inside and outside of the ship. Width and height of the model ship is 0.6 m, and 0.5 m, respectively. The detail is illustrated in **Fig. 9**. The bottom plate of the ship is horizontally flat, submerged in water at a draft of 50 mm. In towing set-up, the bottom is always controlled horizontal without slope. The front edge of the plate was machined by 45 degree to prevent flow separation. A tripping wire was set near the front edge to ensure reproducibility of the spatial development of turbulent

boundary layer. If the wire was not set, the boundary layer begins with laminar state because of the smoothness of the plate and irregularly transits to turbulent state due to uncontrolled perturbation in water. Nominal wall roughness of the acrylic resin made of casting is 10 nm so that the surface is regarded as sufficiently smooth enough relatively to the viscous sublayer thickness of around 10 μm. The hydrofoil was set 650 mm downstream of the leading edge. Three cameras were set to capture the bubble image in different directions: an underwater camera (GoPro HERO3, Gopro Inc., covered with water-resist casing, 120 fps in frame rate), a handy digital video camera (Sony, 60 fps in frame rate), and a high-speed video camera (FASTCAM Mini UX100, Photron Co. Ltd., 500 fps in frame rate, 1/10000 in shutter speed).

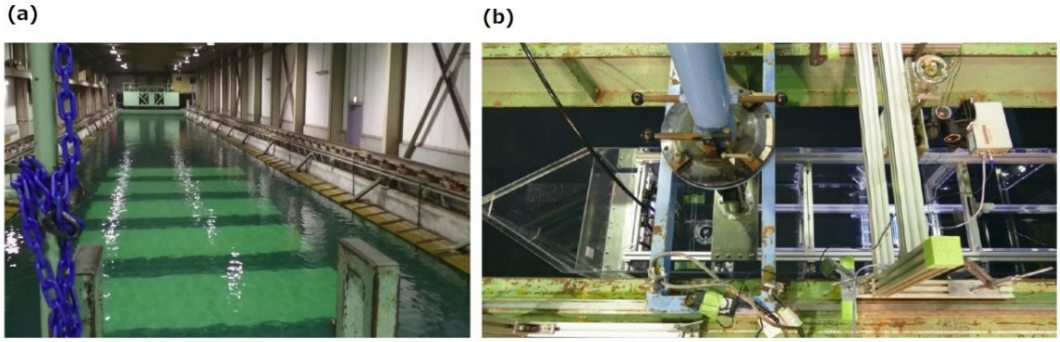

Fig. 8 Towing system for a flat-bottom model ship equipped by hydrofoil bubble generator. (a) 100 m-towing water canal in Hiroshima University, (b) a top view of the model ship attached on the moving train

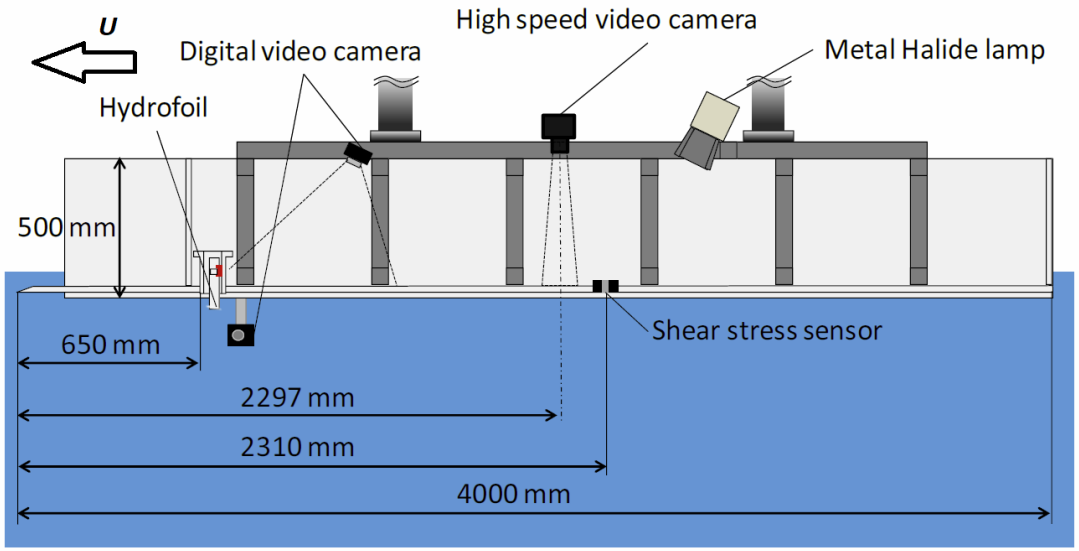

Fig. 9 Measurement set-up for the flat-bottom model ship made of fully transparent acrylic resin

To measure drag acting on the hydrofoil, a principle of lever was applied as illustrated in **Fig. 10**. The hydrofoil is fixed at the bottom edge of a rectangular plate of which top is connected to a rotation support. An axial piezo transducer (DynPick: WDF-6A2004, Wacoh, Ltd., sampling frequency at 2 kHz) was set on a casing near the rotating support, which measures the force acting on the plate. According to the flow visualization results, we set the hydrofoil

depth at h=25 mm (h*=0.5) in this towing experiment. All experimental conditions we carried out are summarized in **Table 2**. We examined two kinds of hydrofoil the same as in previous section, i.e. NACA0012 and NACA4412.

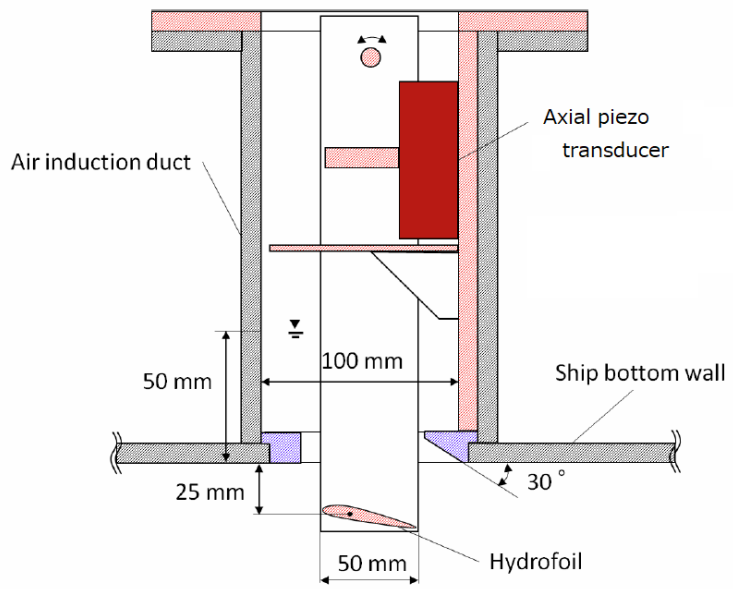

Fig. 10 Measurement method of hydrofoil drag during bubble generation using axial piezo transducer. The hydrofoil is attached on a rectangular plate connected with a rotating support.

Table 2

Experimental conditions of flat-bottom model ship

	Symbol	Value	unit
Towing speed	U	1.50 — 3.00	m/s
Angle of attack	α	10, 15, 20	degree
Temperature		22.8 — 24.3	°C
Water depth (Ship)	H	50	mm
Water depth (Hydrofoil)	h	75	mm
Gap ratio	h*	0.5	-
Reynolds number	Re	0.79×10^5 — 1.60×10^5	-
Froude number (c)	Fr_c	2.2 — 4.3	-
Froude number (h)	Fr_h	1.7 — 3.5	-
Adopted hydrofoil	**Symmetric hydrofoil (NACA0012)**	**Asymmetric hydrofoil (NACA4412)**	

3-2. Bubble generation patterns

Snapshots of bubbles taken by the underwater camera are shown in **Fig. 11**. At U=1.5 m/s for symmetric hydrofoil at α=20 degree, bubbles were not produced (**Fig. 11(a)**). Using the asymmetric hydrofoil at α=10 degree, air-water interface expanded and leaked behind the hydrofoil to release bubbles downstream (**Fig. 11(b)**). The shape dependence is explained by pressure coefficient on the suction surface of the hydrofoil. As Kumagai et al. (2015)

derived, the critical speed of ship, U_c, to start bubble generation can be estimated from Bernoulli's theorem as

$$U_c = \sqrt{\frac{2gH}{|C_p|_{\max}}}, \qquad C_p = \frac{p - p_0}{\rho U^2 / 2}, \qquad p_0 = p_a + \rho g H \ , \tag{7}$$

where C_p is pressure coefficient of the hydrofoil, and p_0 is absolute pressure of water at depth of the hydrofoil. The speed is calculated to be U_C=1.6 m/s for C_p= -0.4 (NACA0012, α=20 deg.) and U_C=0.9 m/s for C_p= -1.1 (NACA4412, α=10 degree). Thus, the theory well explains the result observed at U=1.5 m/s. Increasing the speed up to U=3.0 m/s, the air-water interface was elongated far downstream and many small bubbles were produced in both types of the hydrofoil (**Fig. 11(c) (d)**). However, we saw bubbles trapped steadily above the symmetric hydrofoil at α=20 degree (**Fig. 11(c)**). In contrast, we found wave-breaking at the end of long air-water interface at which fine bubbles were suddenly generated and transported continuously to the downstream region (**Fig. 11(d)**).

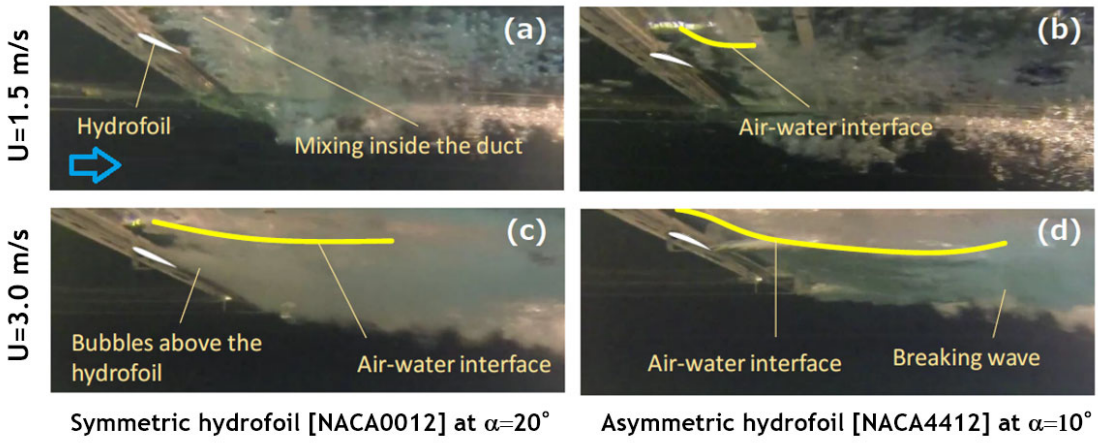

Fig. 11 Underwater snapshot of bubbles generated behind two kinds of the hydrofoil. (a) and (b): low-speed operation producing bubbles downstream intermittently, (c) the hydrofoil fully surrounded by bubbles, and (d) the case of long air-water interfaced formed downstream followed by breaking wave that generates small bubbles. Yellow curves indicate the time-averaged air-water interface estimated from the movie.

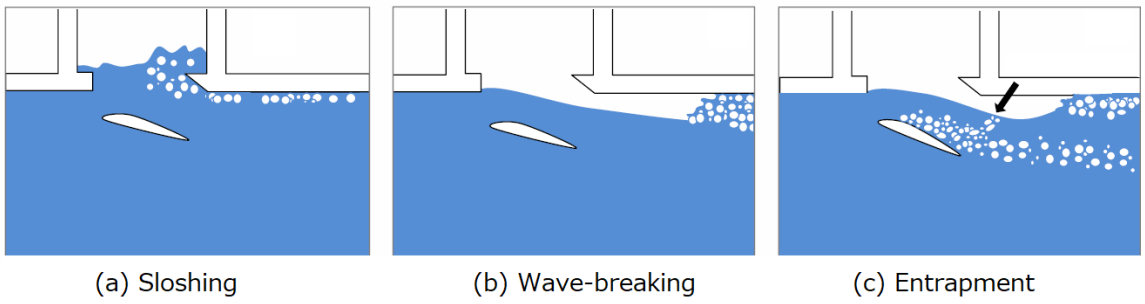

Fig. 12 Ship-speed dependence of bubble generation pattern. (a) Sloshing inside the duct releasing bubbles irregularly, (b) wave-breaking provided by spacing of atmospheric air path and downstream hydrostatic pressure, (c) entrapment of air to the hydrofoil. Spanwise structure was confirmed uniform in any case except the local 3D effect near the wave-breaking point.

Summarizing the observed results, there are three major patterns identified as below and illustrated in **Fig. 12**. (a) Sloshing of air-water interface occurs inside the duct when the flow speed is slow. Bubbles are mostly recirculating just inside the duct and sometime small amount of bubbles are irregularly emitted to the bottom of the plate. (b) Wave-breaking is observed as the speed is raised. A wide air path is provided between the hydrofoil and the ship bottom plate. The wave-breaking brings plenty number of small bubbles conveyed downstream, and its necessary air volume flow rate is stably supplied through the air path. (c) Entrapment of bubbles above the hydrofoil occurs when angle of attack is at 20 degree. This occurs due to cancelation of vertical pressure gradient, which we explained in section 2.5. Once bubbles are accumulated, flow around the hydrofoil alters to be stall state and loses the negative pressure. This results in wave-breaking significantly calmed to reduce bubble generation. It is noted that entrapped bubbles are released downstream intermittently. However, these bubbles are transported away from the wall, and become ineffective for drag reduction.

Changing the flow speed U and the angle of attack α, we made flow pattern diagram as indicated in **Fig. 13**. Abscissa is normalized by Froude number, Fr_c. In case of asymmetric hydrofoil (**Fig. 13 (a)**), three patterns took place; sloshing, wave-breaking and entrapment. Transition from sloshing to wave-breaking depends only Fr_c. This simply obeys Eq. (7), which can be rewritten by transitional Froude number as

$$Fr_C = \frac{U_c}{\sqrt{gC}} = \sqrt{\frac{2H}{C \cdot |C_p|}} = \sqrt{\frac{2 \times 0.075}{0.050 \cdot |C_p|}} \approx 2.5 . \tag{8}$$

Therefore, the negative pressure coefficient of the suction surface of the hydrofoil was estimated to be C_p= - 0.48.

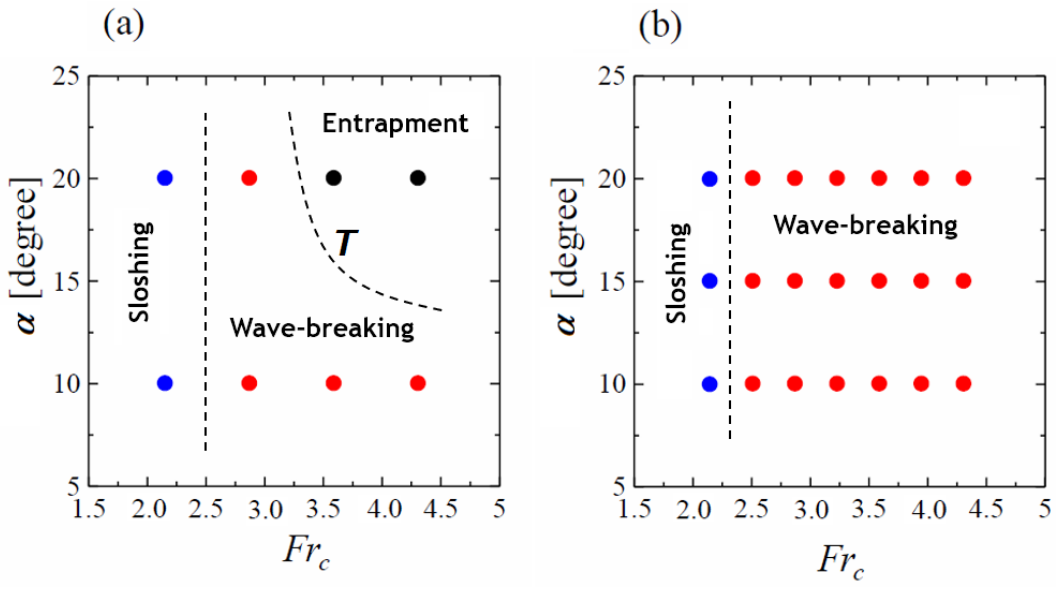

Fig. 13 Interfacial flow patterns dependent on Froude number and angle of attack. (a) Symmetric hydrofoil of NACA0012 having three kinds of flow patterns, (b) Asymmetric hydrofoil of NACA4412 having two kinds of flow patterns emerged.

Transition from wave-breaking to entrapment occurs on a curve in the diagram as indicated by "*T*" in **Fig. 13 (a)**. The transition condition is explained from Eq. (6) as the curvature radius *R* is approximated using the angle of attack α, as

$$Fr_R = \sqrt{\frac{C}{R}} Fr_C > 1, \quad R = \frac{\sin(\alpha/2)}{1-\cos(\alpha/2)} C \quad \rightarrow \quad Fr_C > \sqrt{\frac{R}{C}} = \sqrt{\frac{\sin(\alpha/2)}{1-\cos(\alpha/2)}}. \tag{9}$$

This formula estimates the transitional Froude number as Fr_c=4.8 at α=10 deg., and Fr_c=3.4 at α=20 degree, well matching the results. To avoid bubble entrapment, Eq. (9) teaches that α should be restricted small so that Fr_c can increase to allow high-speed operations.

For the asymmetric hydrofoil, two patterns were observed (**Fig. 13 (b)**). Sloshing appears regardless to angle of attack. This occurs due to instability of air-water interface inside the duct near the downstream edge, which is enhanced by convex surface of the asymmetric hydrofoil. At Fr_c >2.3, it transits to wave-breaking mode, a little bit earlier than the case of symmetric hydrofoil because of large $|C_p|$ effect.

3-3. Bubble generation performance

In this section we present quantitative performance of bubble generation measured by image processing. **Fig. 14** arranges various bubble images taken by the high-speed camera located at 1,650 mm (33*C*) downstream the hydrofoil. Backlighting technique was used so that bubbles are recorded as shadow images. In any case, increase in Fr_c number makes bubbles increase and small. Setting at α=20 deg. generated bubbles more than the case of α=10 degree. Comparing **Fig. 14 (a)** and **(b)**, use of asymmetric hydrofoil produced bubbles more than the symmetric hydrofoil.

Bubble size strongly depends on the flow speed *U*, ranging from 5 mm at *U*=1.5 m/s to a sub-milli meter at *U*=3.0 m/s. The bubble size is estimated from shear Weber number as

$$We_c = \frac{\rho d_c \Delta u^2}{\sigma}, \quad \Delta u = \frac{U}{\delta} d_c \quad \rightarrow \quad d_c = \left(\frac{\sigma \delta^2}{\rho U^2} We_c \right)^{1/3}, \tag{10}$$

where δ and σ are boundary layer thickness and surface tension, respectively. Δu is differential velocity of liquid around a bubble subject to a shear rate scaled by U/δ. Critical Weber number We_c is given by 10, over which bubble begins fragmentation. From this formula, the critical bubble diameter survived in shear is estimated to be d_c=4.2 mm at *U*= 1.0 m/s, d_c=2.6 mm at *U*= 2.0 m/s, and d_c=2.0 mm at *U*= 3.0 m/s. Since bubbles have coalescence and fragmentation centering these sizes, bubbles take the peak population around d_c. This well corresponds to the recorded images of bubbles. Thus, bubble size simply depends on the mean shear rate of the boundary layer and does not depend on the setting condition of the hydrofoil in the far downstream region.

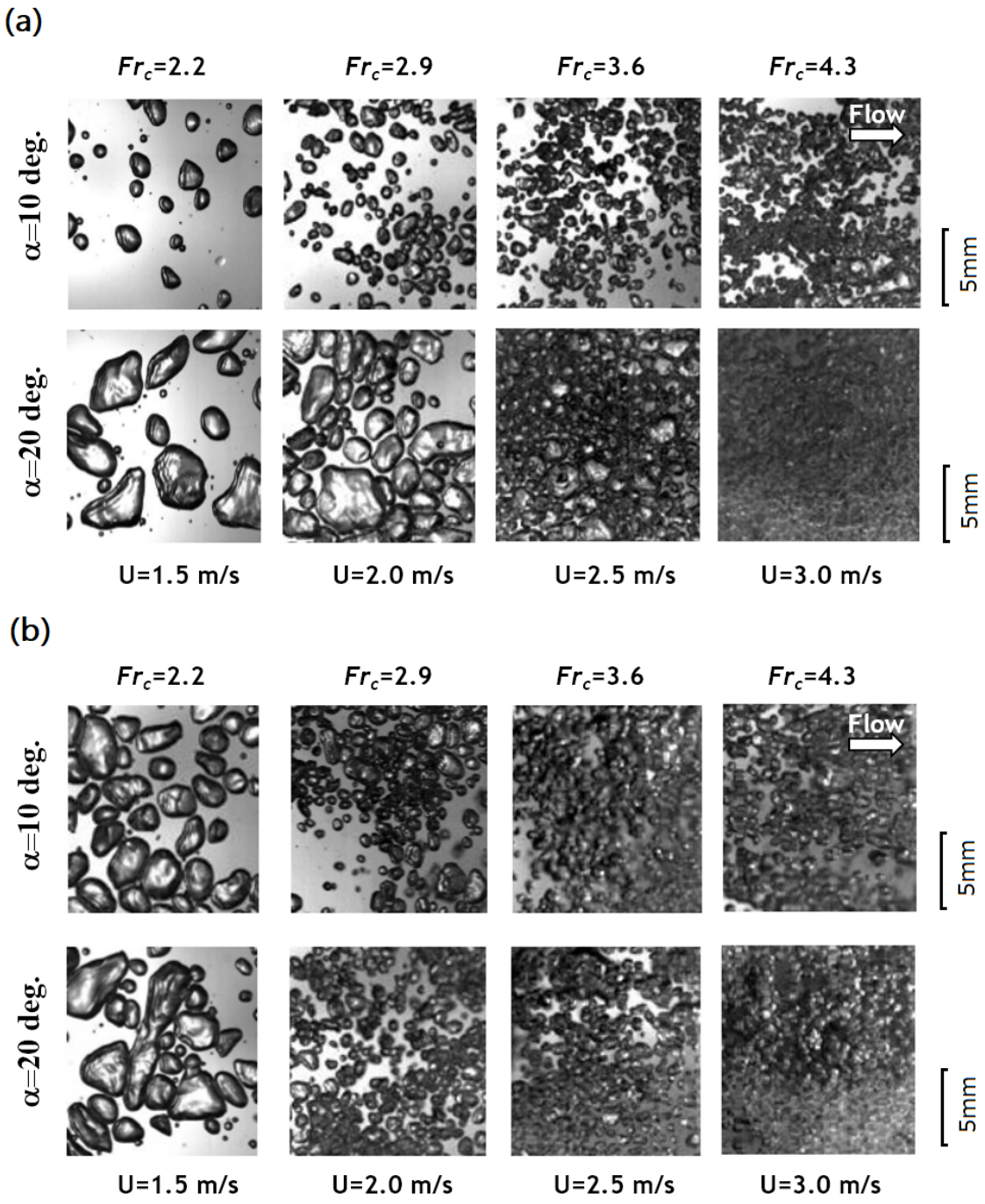

Fig. 14 Top-view snapshots of bubbles just behind the hydrofoil. (a) Symmetric hydrofoil of NACA0012, (b) Asymmetric hydrofoil of NACA4412

To evaluate void fraction, we made image processing composed of three steps as shown in **Fig. 15**. The original image (a) is filtered by a 3x3 pixel median filter to remove pixel-by-pixel noise (b), and binarized using a threshold value to extract individual bubble interfaces (c), and then converted to bubble images with fill-holes operation (d). From this converted image, projection void fraction of bubbles β, which is defined by

$$\beta = \frac{A_b}{A}, \quad A_b = \int_x \int_y a(x,y) \cdot dxdy, \quad A = \int_x \int_y 1 \cdot dxdy \,, \tag{11}$$

is measured where $a(x,y)$ is a binary function giving a=1 inside gas phase and a=0 inside liquid phase in the recorded image. Hence, β means the ratio of wall occupation by bubbles to all the examined area. **Fig. 16** shows the time-averaged result of β taking from 2,000 consecutive images. It is confirmed that β increases with the flow speed U or Fr_c number. At α=10 degree, the asymmetric hydrofoil produces β larger than the symmetric hydrofoil. This trend is reversed at α=20 degree. For the angle of attack α=15 deg., we omitted measurement because of time limitation for the 100 m towing experimental period allowed.

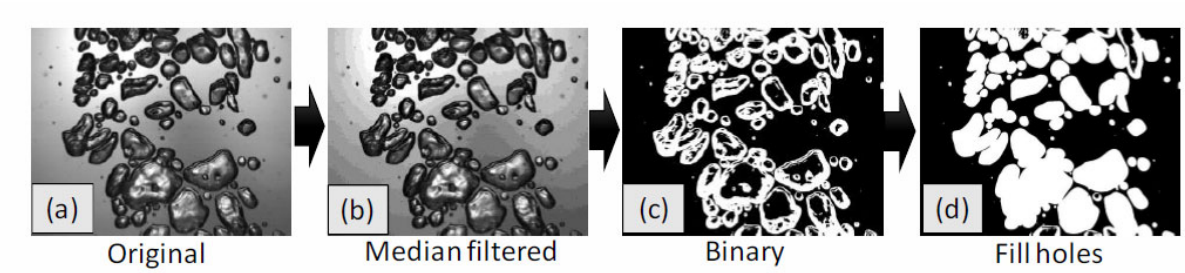

Fig. 15 Image processing for measuring the projection void fraction define by Eq. (11) with three sequential processing via median filtering, binarization, and fill-holes processing. The sampling image size is 120 mm x 120 mm to define the local instantaneous projection void fraction.

Bubble advection velocity also takes the similar trend as shown in **Fig. 17**. The velocity was measured by one-dimensional cross correlation analysis as like PIV applied for bubble shadow images. The mean bubble velocity U_b was ranged from 0.4U to 0.8U, inferring that these bubbles are suspended inside the turbulent boundary layer. Note that the velocity was obtained slower than 0.4U in the case of α=20 degree for the symmetric hydrofoil. This associates with bubble entrapment above the hydrofoil, which intermittently produces large air films creeping close to the wall slowly. For the angle of attack α=15 deg., we omitted measurement because of time limitation for the 100 m towing experimental period allowed.

Using the measured values of projection void fraction β and mean bubble velocity U_b, bubble volume flow rate passing by the measurement section is estimated using the following relation,

$$Q_t = \beta\delta_b W \cdot U_b \quad [\mathrm{m}^3/\mathrm{s}], \qquad Q = \frac{Q_t}{W} = \beta\delta_b \cdot U_b \quad [\mathrm{m}^2/\mathrm{s}], \tag{12}$$

where δ_b is bubble suspended layer thickness inside the boundary layer. Q_t is total bubble volume flow rate generated by a single hydrofoil with a spanwise length W. We evaluate here Q without suffix, which is the bubble volume flow rate per unit spanwise length. It is noted that $\beta\delta_b$ in above equations is known to be equivalent air-layer thickness, t_a, so called in past reports on air lubrication ships. In evaluation of δ_b, position of bubble's bottom interface from the wall is known insensitive to bubble size and coincides with border of the boundary layer (Oishi and Murai, 2014). Regarding the position of bubble's top interface, Park et al. (2019) measured it to confirm matching with the border of buffer layer thickness, i.e. less than 1 mm in water flow. Furthermore, our past experiments using the same model ship indicated that the bubble suspended layer thickness was half of the turbulent boundary thickness defined by momentum thickness (Park et al. 2015; Park et al. 2018). Upon these knowledges, the mean bubble height is assumed

to be δ_b =10 mm in this study.

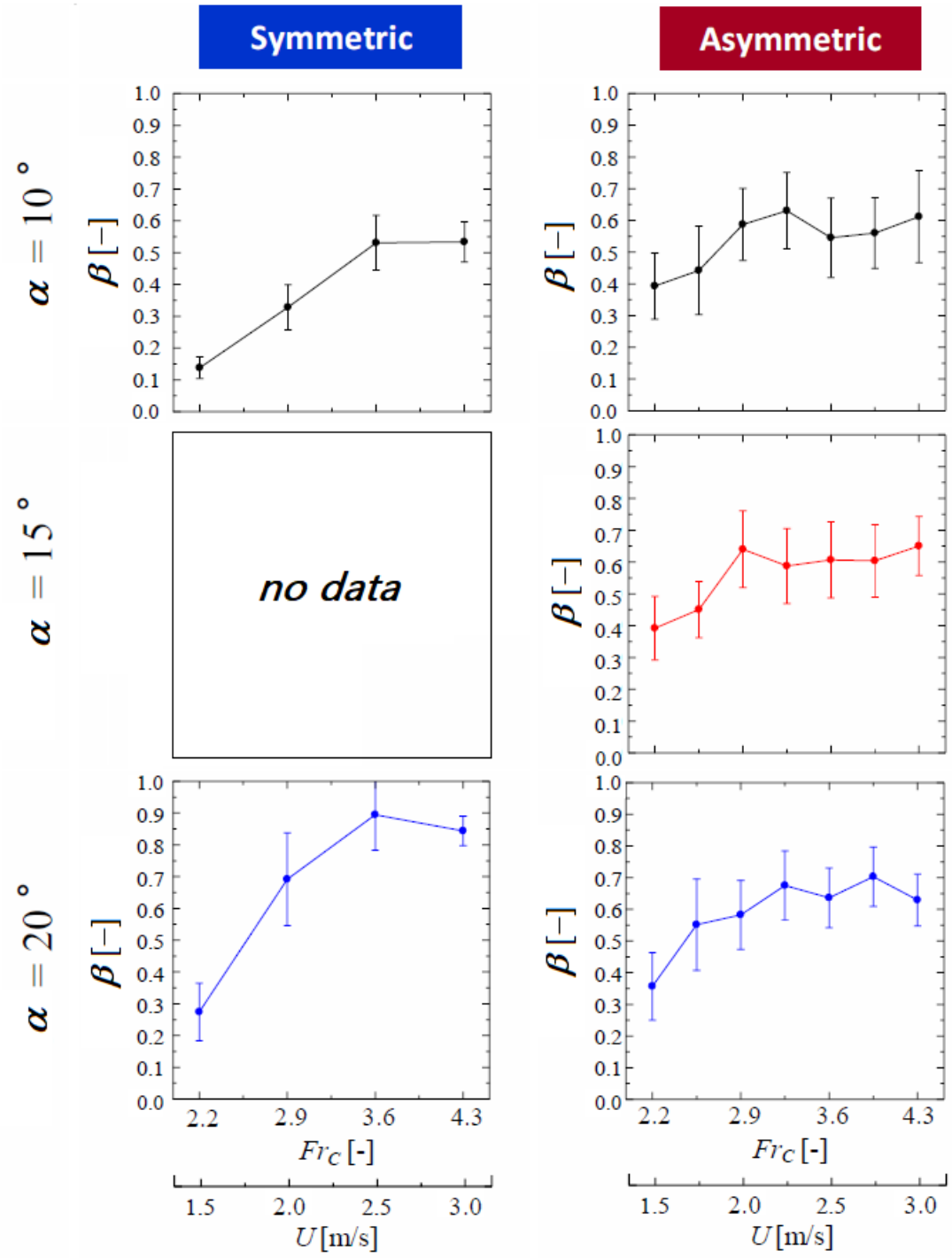

Fig. 16 Projection void fraction of bubbles increasing with the ship speed U. Each plot is time-averaged value for 2,000 consecutive image frames (4.0 sec.) while the bars stand for the standard deviation which is strongly influenced by bubble fragmentation and coalescence inside the boundary layer.

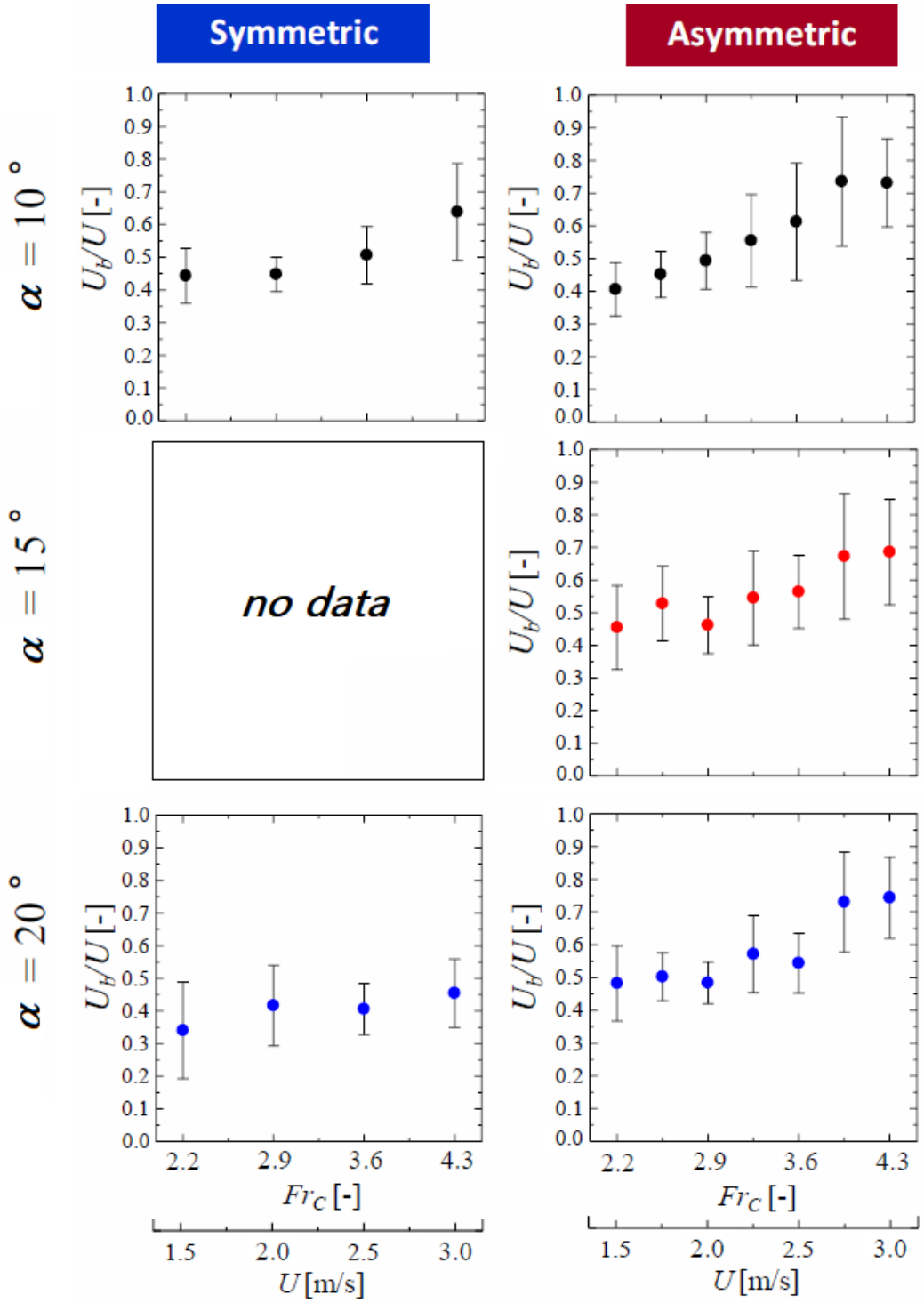

Fig. 17 Time-averaged bubble advection velocity relative to ship speed, which tends to increase with Fr_C. The bars indicate the standard deviation within the sampling period of 4.0 seconds.

Fig. 18 plots the bubble volume flow rates per unit spanwise length, Q. In any condition, Q increases monotonically with the flow speed, U. For the symmetric hydrofoil, Q increases linearly with U. In this case, there is an onset flow speed for bubble generation around U=1.3 m/s, which corresponds to transition from sloshing mode

to wave-breaking mode as previously explained. In contrast, the asymmetric hydrofoil generates bubble flow rate upon a power law to U. By least square fitting, the exponents are found to be larger than two. That is, the more the ship speed increases, the much more the bubbles are generated to promote drag reduction. We consequently obtained the experimental formula of bubble volume flow rate for the asymmetric hydrofoil to be

$$\begin{aligned} Q(\alpha,U) &= Q_\alpha \left(U/U_0\right)^P \qquad [\mathrm{m^2/s}] \\ Q_\alpha(\alpha) &= \left(-0.0051\alpha^2 + 0.263\alpha - 1.195\right)\times 10^{-3} \qquad [\mathrm{m^2/s}], \\ P(\alpha) &= 0.0078\alpha^2 - 0.241\alpha + 4.11 \qquad [-] \end{aligned} \tag{13}$$

which is valid for $10<\alpha<20$ deg., and $1.5<U<3.0$ m/s. Units for Q, U and α should be $\mathrm{m^2/s}$, m/s, and degree, respectively in the above formula. U_0 is a reference flow speed defined at U_0= 1 m/s. Note that installment of an air flowmeter significantly reduced the bubble generation rate. This was because the air of atmospheric pressure is naturally introduced to the water above the hydrofoil without pressure difference in the present system (in principle, zero-pressure gradient).

From Eq. (10) and Eq. (13), number of bubbles generated in unit spanwise length and in unit time, i.e. bubble number flux, is estimated as

$$n_b = \frac{Q}{\pi d_c^{\,3}/6} = \left(\frac{6\rho}{\pi\sigma\delta^2 We_c}\right) QU^2 = 2.6\times 10^7 \cdot QU^2 \quad [1/\mathrm{sm}]. \tag{14}$$

If we use average exponent of U for $10<\alpha<20$ deg., which is P = 2.35, Eq. (14) means the bubble number flux being increased with the flow speed, $n_b \propto U^{2+2.35} = U^{4.35}$. The dramatic change of bubble distributions with the flow speed, which was visualized in **Fig. 14**, is now explained with this great exponent. Namely, twice the flow speed from U=1.5 to U=3.0 m/s made the number of bubbles $2^{4.35}$=20 times multiplied. This is a great advantage of the hydrofoil-type bubble generator in comparison with pressurized air blowing. Because the blowing is usually operated at Q=constant, the exponent of U in Eq. (14) remains as two. The hydrofoil system can naturally breed the bubbles with increase in the ship speed.

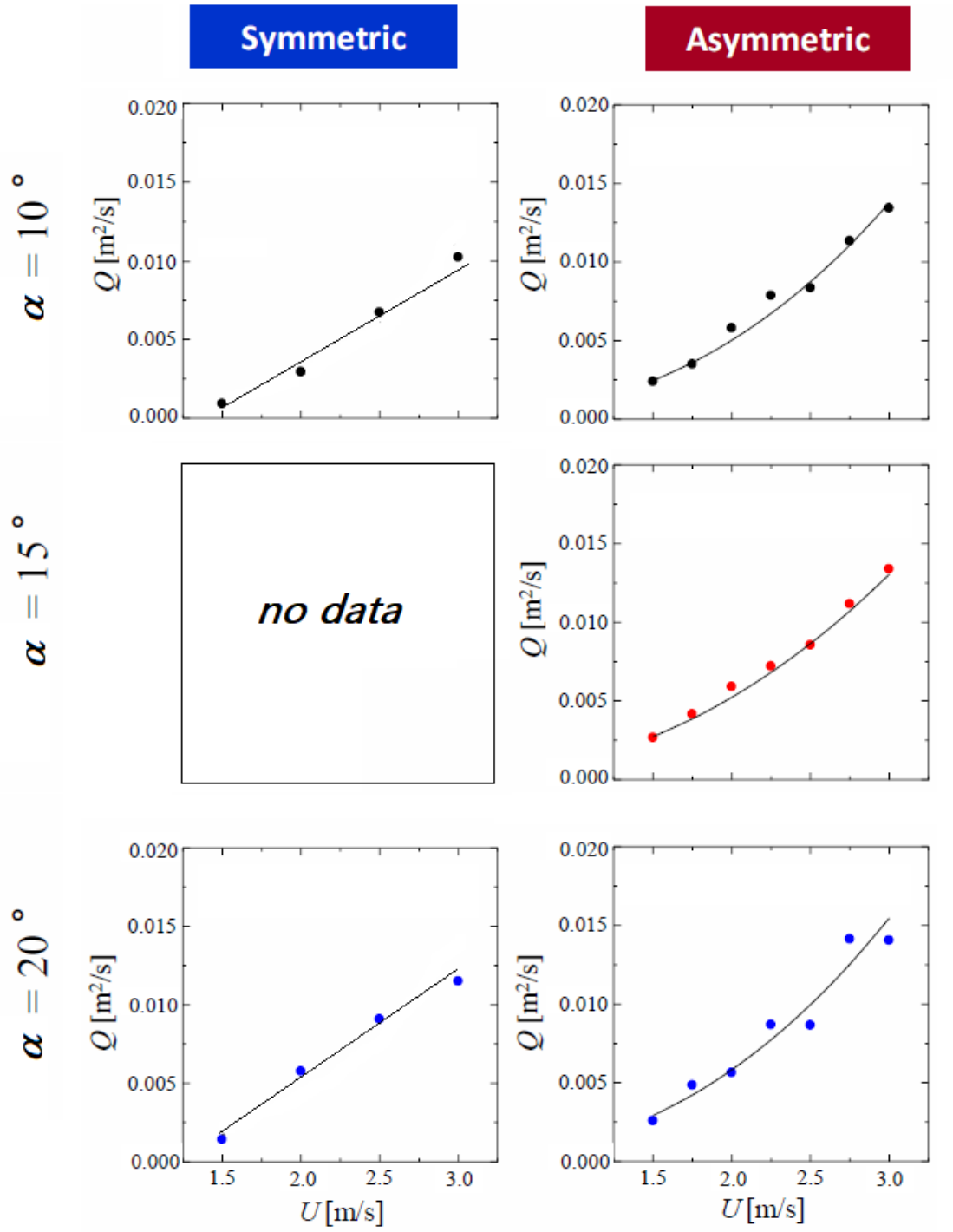

Fig. 18 Bubble volume flow rate produced by the hydrofoil

3-4. Drag of hydrofoil in operation

While drag coefficients of NACA type hydrofoils/airfoils were well investigated, those in the conditions generating bubbles were not clarified. Drag coefficient of the hydrofoil is defined by

$$C_D = \frac{D}{\left(\rho U^2 / 2\right) \cdot CW}, \tag{15}$$

where D is drag force directly acting on the hydrofoil, measured by the piezo transducer. C and W are the cord length and the spanwise length of the hydrofoil. In this definition, we do not normalize D with neither the angle of attack, the hydrofoil depth, upheaval/caving of free surface, nor bubble entrapment. These factors are treated as resultant modification of C_D.

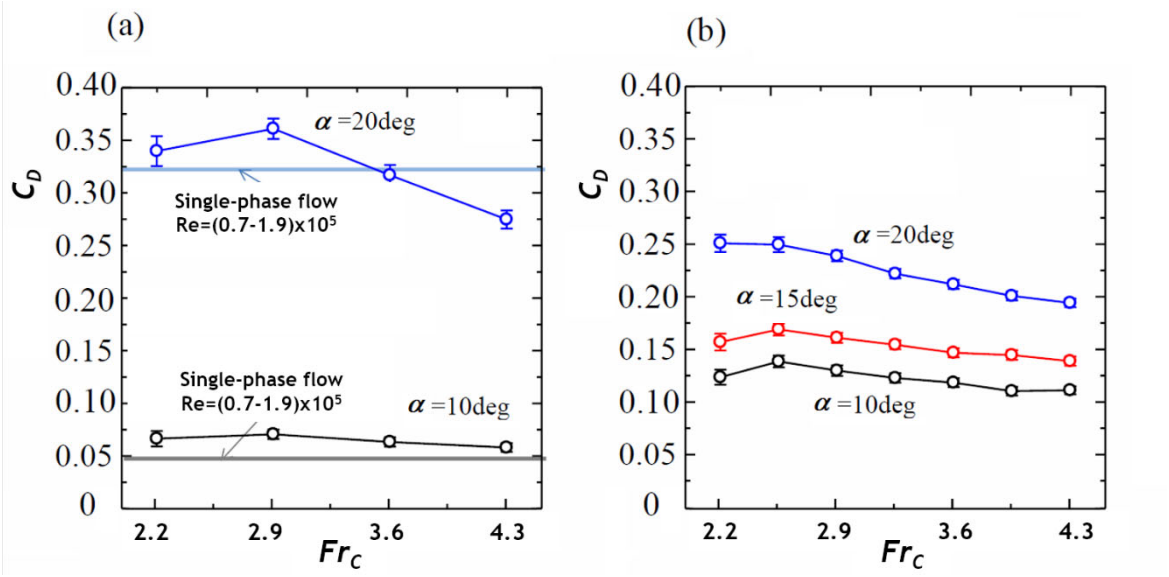

Fig. 19 Drag coefficient of the hydrofoil during bubble generation at H/C=1.5. (a) Symmetric hydrofoil of NACA0012 compared with the drag of single-phase applications, (b) Asymmetric hydrofoil of NACA4412

Fig. 19 plots measured result of C_D as a function of Fr_c number at H/C=1.5. In the case of symmetric hydrofoil (Fig. 19 (a)), drag jumped up as the angle of attack changes from 10 to 20 degree due to flow separation (stall) at 20 degree. This corresponds to the increase of the drag in single-phase infinite flow as indicated by straight lines. At α=10 deg., drag in two-phase flow was always larger than that in single-phase flow. This is due to drag enhancement by bubble generation. At α=20 deg., drag decreased lower than that of single-phase flow at Fr_c >3.5. This trend is explained by anti-stall effect due to free surface approaching the hydrofoil and reduction of inertia. For the asymmetric hydrofoil (Fig. 19 (b)), drag difference due to the angle of attack was reduced. Increase of Fr_c made the drag decrease at Fr_c >2.5. This region corresponds to the wave-breaking regime (Fig. 13), i.e. air-water interface is smoothly elongated along the convex surface of the hydrofoil.

3-5. Estimation of power efficiency

In this section we evaluate the feasibility of the hydrofoil bubble generator for real-scaled marine vessels. First of all, power efficiency of the hydrofoil as a bubble generator can be defined by

$$\eta = \frac{P_b}{P_C}, \quad \begin{cases} P_b = \rho g H Q \cdot W \\ P_C = C_D \cdot \frac{1}{2} \rho U^3 \cdot CW \end{cases} \tag{16}$$

where nominator P_b is the necessary power to inject bubbles into water at which hydrostatic pressure ρgH acts. H is the depth of the bubble injection point from sea surface. Q is the bubble volume flow rate per unit spanwise length, and W is the spanwise length of the hydrofoil. The denominator P_C is the power consumed for the hydrofoil drag,

which is proportional to U^3. In Eq. (16), Q and C_D are given as functions of the Froude number Fr_c and the angle of attack α, using the data of Fig. 18 and Fig. 19. Substituting all the experimental data for these two values, overall power efficiency η has been obtained as shown in **Fig. 20**. It takes the values in the range of 3 to 15%. In the case of symmetric hydrofoil, the efficiency had an increasing trend with Fr_c (**Fig. 20 (a)**). The trend was reversed in the case of the asymmetric hydrofoil (**Fig. 20 (b)**). For both hydrofoils, the smaller the angle of attack, the higher the power efficiency is improved. This recommends use of small angle of attack as a single unit of bubble generator if we weight on the power efficiency. However, whole system performance should be evaluated considering downstream BDR performance as we estimate next.

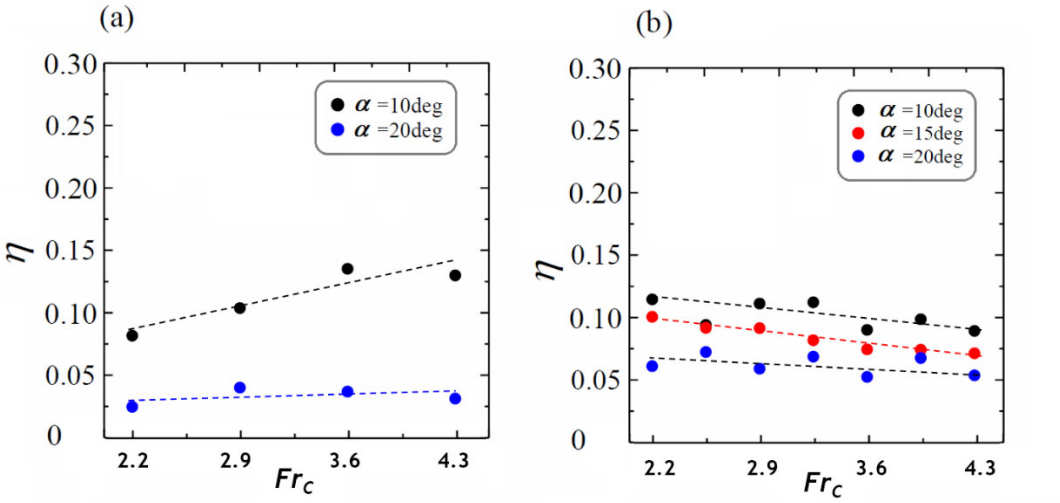

Fig. 20 Power efficiency of bubble generation at h^*=0.5. (a) Symmetric hydrofoil of NACA0012, (b) Asymmetric hydrofoil of NACA4412. Straight broken lines indicate linear fitted trends of plots in each condition.

Hereafter we estimate the gross effect of the hydrofoil for obtaining drag reduction. Reduction of local friction coefficient ΔC_f is approximated by the following function (e.g. Watanabe et al., 1998),

$$\Delta C_f(x) = \frac{\Delta \tau_w(x)}{\rho U^2/2} = C_{f0}(x)\left(1 - \frac{a}{x+b}\right), \tag{17}$$

where x is the downstream distance from the bubble injector and $C_{f0}(x)$ is original profile of the friction coefficient. The constants a and b, which have a length scale, describes all the effect of BDR such as accumulation of bubbles due to buoyancy and diffusion of bubbles away from the wall due to turbulence. These constants also depend on geometry of hull such as slope and curvature of the target surface. From this function, total drag reduction is estimated as

$$\Delta D = \int_0^L \Delta \tau_w(x) \cdot W dx = \frac{1}{2}\rho U^2 W \int_0^L C_{f0}(x)\left(1 - \frac{a}{x+b}\right) \cdot dx, \tag{18}$$

where L is the total downstream distance of the hull. Hence the power-saving by the drag reduction is estimated by

$$P_{DR} = \Delta D \cdot U = \frac{1}{2}\rho U^3 W \int_0^L C_{f0}(x)\left(1 - \frac{a}{x+b}\right) \cdot dx. \tag{19}$$

Therefore, net gain of the power-saving by the hydrofoil bubble injector can be evaluated as

$$\xi = \frac{P_{DR}}{P_C} = \frac{1}{C_D \cdot C}\int_0^L C_{f0}(x)\left(1-\frac{a}{x+b}\right)\cdot dx\,. \tag{20}$$

If the gain ξ is larger than unity, equipment of hydrofoil provides net power-saving. According to the results of drag reduction reported by Kumagai et al. (2015) and Park et al. (2018), the constants a and b for a flat bottom hull can be modeled by

$$a = 2.6\left[1-\exp\left(-230\frac{Q}{Q_0}\right)\right], \quad b = 2.6\ , \tag{21}$$

at α=20 degree for the asymmetric hydrofoil, where Q_0 is a reference flow rate given by Q_0= 1 m^2/s. C_{f0} of the turbulent boundary layer without bubbles described by

$$C_{f0} = 0.026 Re_x^{-1/7}, \quad Re_x = \frac{Ux}{\nu} > 3\times 10^5, \tag{22}$$

and C_D at α=20 degree is modeled from the present data as

$$C_D = 0.33 Fr_C^{-0.32} \quad , Fr_C > 2.5\,. \tag{23}$$

The bubble volume flow rate at α=20 degree is given from Eq. (13) as

$$Q = 1.1\times 10^{-3}\left(\frac{U}{U_0}\right)^{2.41}\,. \tag{24}$$

Substituting these models and fluid properties to Eq. (20), the net gain is obtained as functions of flow speed U and the ship length L, as

$$\xi(U,L) = 1.80\left(\frac{U}{U_0}\right)^{0.32}\int_0^L\left(\frac{Ux}{\nu}\right)^{-1/7}\left\{1-\frac{2.6}{x+2.6}\left[1-e^{-0.253\left(\frac{U}{U_0}\right)^{2.41}}\right]\right\}\cdot dx\,, \tag{25}$$

where U_0= 1 m/s and ν=10^{-6} m^2/s are applied as referential values for non-dimensionalization of each term.

Table 3

Estimation of net gain factor ξ of hydrofoil bubble injector for ship drag reduction

		Ship speed U[m/s]									
		1	2	3	4	5	6	7	8	9	10
Ship length L [m]	2	0.4	0.2	0.2	0.2	0.2	0.2	0.2	0.2	0.2	0.2
	4	0.8	0.6	0.4	0.4	0.5	0.5	0.5	0.5	0.5	0.5
	8	1.5	1.2	1.1	1.1	1.2	1.2	1.2	1.3	1.3	1.3
	16	2.8	2.6	2.5	2.6	2.7	2.8	2.8	2.9	3.0	3.0
	32	5.3	5.2	5.2	5.4	5.6	5.8	6.0	6.1	6.3	6.4
	64	9.7	10.1	10.4	10.9	11.3	11.7	12.0	12.3	12.6	12.8
	128	17.9	19.2	20.1	21.1	22.0	22.7	23.3	23.9	24.4	24.8
	256	32.7	35.8	37.9	39.9	41.5	42.8	44.0	45.1	46.0	46.9

By numerical integrating the r.h.s. of Eq. (25) respect to x for overall distance L, the net gain was calculated as listed in **Table 3**. In case of the ship length L>8 m, the gain takes the value higher than unity. This means BDR effect overcomes hydrofoil drag. At L>64 m, the gain is amplified larger than 10. The ship speed U influences the gain non-monotonically at L<32 m. In ordinary cruising speed of commercial ship at 4<U<8 m/s, the gain increases with the speed U. This is attributed to the Froude number dependency of hydrofoil drag (Eq. (23)) and high-exponent power law characteristics of the bubble volume flow rate to the ship speed (Eq. (13) or Eq. (24)).

Of course, we need to consider 3D hull surface for further exact estimation. For example, Air Cavity Ship (ACS) is designed for a planning hull utilizing depressurizing effect of the boundary layer. Bubble generation performance will change in such a 3D flow environment. Eq. (25) is just to estimate one-dimensional performance along a horizontally flat-bottom hull. In our previous report (Kumagai et al. 2015), arrangement of the hydrofoils was decided considering 3D streamlines of water on hull surfaces. If we extend Eq. (25) applicable to curved and non-horizonal hull surfaces, the present theory will be able to predict the optimum arrangement of the hydrofoils for arbitrary figure of the hull to cover widest surface with bubbles. This should be positioned as the next target of our study.

5. Conclusion

In this paper we reported on the mechanism and the performance of a hydrofoil bubble generator. Purpose of the present experiment was to find the answers for the questions we declared in the introduction. For each question, the following points have been made clear. i) Why can hydrofoil effectively generate bubbles? - The bubble generation relied on negative pressure induced above the hydrofoil. It sucked in atmospheric pressure to the air path provided by declined water flow along the hydrofoil surface. Dependent on Froude number, there were three kinds of flow patterns identified as shown in **Fig. 12**. Among them, wave-breaking mode produced largest amount of bubbles due to flash-flow accelerating straightly toward the wave-breaking point. ii) What kind of hydrofoil shape works better as bubble generator? – By comparing the flows of NACA0012 and NACA4412 hydrofoils, asymmetric hydrofoil generated bubbles more at high Froude number. The bubble volume flow rate increased with the flow speed to the power of greater than two. Drag acting on the asymmetric hydrofoil during bubble generation was smaller than that on the symmetric one at 20 degree in the angle of attack. iii) How the resultant bubble volume flow rate of bubbles can be estimated? – By measuring void fraction and bubble velocity, the bubble volume flow rate per unit spanwise length of the hydrofoil was formulated with Eq. (13) as a function of angle of attack. This allowed us to estimate the power efficiency of the bubble generator as a pump, and it was in the range of 3 to 15%. This led to the net gain of the drag reduction being greater than unity for the ship length longer than 8 m, and being greater than 10 for that longer than 64 m.

In this work, we focused on the hydrofoil's effect beneath a horizontal plate. In the field of Air Cavity Ship (ACS), depressurized effect of planning hulls for bubble introduction is being developed, i.e. the influence of slope and curvature of the hull in water. We might suggest a combined use with it and further effective design of the hydrofoil set-up to propel the spread of BDR technique in future.

Acknowledgment

The work presented in the manuscript was supported by JSPA KAKENHI grant no. 17H01245, and Innovative

Science & Technology Initiative for Security, ATLA, Japan. The authors express thanks to Prof. Hiroki Yasukawa (Hiroshima Univ.), Dr. Yoshiaki Takahashi (WAIP Ltd.), Dr. Yoshihiko Oishi (Muroran Inst. Tech.) and Mr. Toshiyuki Sampo (Hokkaido Univ.).

References

Air lubrication technology (https://ww2.eagle.org/), 2019, American Bureau of Shipping, April 1, 2019, pp. 1-15.

Ceccio, S.L., 2010. Friction Drag Reduction of External Flows with Bubble and Gas Injection, Annu. Rev. Fluid Mech. 42, 183–203.

Cucinotta, F., Guglielmino, E., Sfravara, F., 2017, An experimental comparison between different artificial air cavity designs for a planning hull, Ocean Engineering, 140, pp. 233-243.

Duncan, J. H., 1983. The breaking and non-breaking wave resistance of a two-dimensional hydrofoil. J. Fluid Mech., 126, pp. 507-520.

Fuwa, T., Ishizaka, J., 1980, On the characteristic of a hydrofoil section running at a constant advance speed in calm water, Transaction of Kansai Ship-building society, 178, 69-79 (in Japanese).

Hara, K., Suzuki, T., Yamamoto, F., 2011, Image analysis applied to study on frictional-drag reduction by electrolytic microbubbles in a turbulent channel flow, Experiments in Fluids, 50, pp. 715-727.

Jang, J., Choi S-H., Ahn S-M., Kim B., Seo J-S., 2014. Experimental investigation of frictional resistance reduction with air layer on the hull bottom of a ship. Int. J. Nav. Archit. Ocean Eng., 6, pp. 363-379.

Kitagawa, A,, Denissenko, P., Murai, Y., 2019, Behavior of bubbles moving along horizontal flat plates with different surface wettability, Experimental Thermal and Fluid Science, 104, pp.141-152.

Kitagawa, A., Hishida, K., Kodama, Y., 2005. Flow structure of microbubble-laden turbulent channel flow measured by PIV combined with the shadow image technique. Exp. Fluids 38, 466–475.

Kumagai, I., Murai, Y., Tasaka, Y., Nakamura, N., 2011. Bubble generation by a cylinder moving beneath a free surface, Journal of Fluid Science and Technology, Vol.6, No.6, 851-859.

Kumagai, I., Takahashi, Y., Murai, Y., 2015, Power-saving device for air bubble generation using a hydrofoil to reduce ship drag: theory, experiments, and application to ships, Ocean Engineering, 95, pp. 183-194.

Mäkiharju, S.A., Lee, I-H. R., Filip, G.P., Maki, K.J., Ceccio, S.L., 2017, The topology of gas jets injected beneath a surface and subject to liquid cross-flow, Journal of Fluid Mechanics, 818, pp. 141-183.

Moriguchi, Y., Kato, H., 2002, Influence of microbubble diameter and distribution on frictional resistance reduction, Journal of Marine Science and Technology, 7, pp. 79-85.

Murai, Y., 2014. Frictional drag reduction by bubble injection. Exp. Fluids 55, 1773 (p.28).

Murai, Y., Fukuda, H., Oishi, Y., Kodama, Y., Yamamoto, F., 2007. Skin friction reduction by large air bubbles in a horizontal channel flow. Int. J. Multiphase Flow 33, 147–163.

Murai, Y., Takahashi, Y., 2008. Frictional drag reduction ship, Patent Number: 4070385 (2008), Japan.

Oishi, Y., Murai, Y., 2014, Horizontal turbulent channel flow interacted by a single large bubble, Experimental Thermal and Fluid Science, 55, pp. 128-139.

Oishi, Y., Tohge, Y., Murai, Y., Tasaka, Y., 2019, Bubble clustering in a horizontal turbulent channel flow investigated via bubble-tracking velocimetry, International Journal of Multiphase Flow, 120, 103104.

Park, H.J., Saito, D., Tasaka, Y., Murai, Y., 2019, Color-coded visualization of microbubble clouds interacting with eddies in a spatially developing turbulent boundary layer, Experimental Thermal and Fluid Science, 109, 109919.

Park, H.J., Tasaka, Y., Murai, Y., 2018, Bubbly drag reduction accompanied by void wave generation inside turbulent boundary layers, Experiments in Fluids, 59, 166.

Park, H.J., Tasaka, Y., Murai, Y., 2019, Bubbly drag reduction investigated by time-resolved ultrasonic pulse echography for liquid films creeping inside a turbulent boundary layer, Experimental Thermal and Fluid Science, 103, pp.66-77.

Park, H.J., Tasaka, Y., Oishi, Y., Murai, Y., 2015, Drag reduction promoted by repetitive bubble injection in turbulent channel flows, International Journal of Multiphase Flow, 75, pp. 12-25.

Pavlov, G.A., Yun, L., Bliault, A., He, S.-L., 2020. Air lubricated and air cavity ships development, design, and application. Springer.

Reichl, P., Hourigan, K., Thompson, M.C., 2005, Flow past a cylinder close to a free surface, Journal of Fluid Mechanics, 533, pp. 269-296.

Sanders, W.C., Winkel, E.S., Dowling, D.R., Perlin, M., Ceccio, S.L., 2006, Bubble friction drag reduction in a high-Reynolds-number flat-plate turbulent boundary layer, Journal of Fluid Mechanics, 552, pp. 353-380.

Sheridan, J., Lin, J-C., Rockwell, D., 1997, Flow past a cylinder close to a free surface, Journal of Fluid Mechanics, 330, pp. 1-30.

Takahashi, Y., Murai, Y., 2014. Friction reducing ship and method for reducing frictional resistance, United States Patent, No. US 6789491B2.

Watanabe, O., Masuko, A., Shirose, Y., 1998. Measurements of drag reduction by microbubbles using very long ship models (in Japanese), J. Soc. Naval Arch. Japan 183, 53-63.

Yanuar, Putra, M.S.G., Akbar, M., Alief, M., Fatimatuzzahra, 2020, Numerical study on influence of hydrofoil clearance towards total drag reduction on winged air induction pipe for air lubrication, International Journal of Technology, 11, pp. 91-99.

Zhang, J., Yang, S., Liu, J., 2018, Numerical investigation of a novel device for bubble generation to reduce ship drag, International Journal of Naval Architecture and Ocean Engineering, 10, pp. 629-643.

Zhen, L., Hassan, Y.A., 2006, Wavelet autocorrelation identification of the turbulent flow multi-scales for drag reduction process in microbubbly flows, Chemical Engineering Science, 61, pp. 7107-7114.